Materials Transactions, Vol. 42, No. 8 (2001) pp. 1710 to 1716

Microstructural Stability of Gas-Atomized Al-Based Nanophase Composites

Jian Qiang Wang[1,2] and Sie Chin Tjong[1,*]

[1]*Department of Physics and Materials Science, City University of Hong Kong, Tat Chee Avenue, Kowloon, Hong Kong, P.R. China*
[2]*State Key Laboratory for Rapidly Solidified Nonequilibrium Alloys, Institute of Metal Research, Chinese Academy of Sciences, Shenyang 110015, P.R. China*

The microstructure evolution and grain growth behavior, of gas-atomized $Al_{88}Ni_9Ce_2Fe_1$ nanocomposite materials, were studied by means of the X-ray diffraction, transmission electron microscopy, and differential scanning calorimetry. The results showed that the microstructure of as-atomized powders are affected by the degree of solute supersaturation in matrix, the microstrain contained, the size, distribution and volume fraction of nanophase precipitated, and these are essentially sensitive to the powder particle sizes. Moreover, there appeared to be a two-stage phase transformation during thermal crystallization, *i.e.*, the precipitation of α-Al and the growth of $Al_3(Ni, Fe)$ nanophase in preference to $Al_{11}Ce_3$ nanophase, respectively. Finally, the grain growth kinetics of α-Al at temperatures of 250 to 300°C, revealed that the volume-diffusion grain growth mechanism with an activation energy of 1.3 eV is controlling in the nanophase materials.

(Received March 21, 2001; Accepted June 4, 2001)

Keywords: *nanocomposite, rapid quenching, microstructure, grain growth*

1. Introduction

A new class of Al-based nanocomposites, with face-centered cubic Al nanocrystals homogeneously dispersed in an amorphous matrix, demonstrate interesting mechanical properties. The tensile strength of composites can reach as high as 1.6 GPa, which is about 1.5 times to that of the corresponding fully glassy alloys and 3 times higher than that of conventional precipitation hardened alloys.[1,2] Such a nanophase composite with high mechanical strength can be achieved by melt-quenching at a rate below the critical value or by annealing an initially amorphous material. The devitrification can also be induced by the mechanical alloying process. The nanostructure frequently obtained from devitrification of various Al–Ln or Al-TM-Ln (where TM represents a transition metal and Ln a lanthanide) metallic glasses appears to exhibit a high nucleation rate and a slow growth velocity. According to the literature, the mechanism and kinetics of developing ultrafine microstructure in several alloy systems still remain unclear and controversial. Several models have been proposed to date. These include nano/amorphous metastable equilibrium,[3] transient heterogeneous nucleation,[4] homogeneous nucleation and diffusion field impingement,[5] the mean-field model for nucleation and diffusion-controlled growth,[6] model fluxes of interface attachment and diffusion.[7,8]

In general, the research studies on the development of ultrafine microstructures in Al-based metallic glasses are focussed in the first stage crystallization reaction. Little attention is paid on its subsequent phase transformation process and structural stability. In fact, an understanding of the whole crystallization process can provide useful information concerning the stability of materials. More recently, consolidated powder products, either partially or fully crystallized, have been found to retain a fine-scale microstructure of interest, hence exhibit superior properties. For example, consolidated alloys of the Al-TM-RE (rare earth) type has a superplastic elongation larger than 500% under a strain rate as high as 1 s^{-1}.[9] Moreover, the mechanical strength ($\sim$ 900 MPa) of such alloys is considerably higher than that of conventional high-strength aluminum alloys.

Spray atomization, a promising process in terms of low manufacturing cost coupled with optimum materials performance, has currently been adopted to produce the Al-based amorphous and/or nanostructural alloy powders. The produced powders are generally densified by hot extrusion or forging. In this paper, we attempt to examine the formation and evolution mechanism of Al–Ni–Ce–Fe nanocomposites produced by ultrasonic gas atomization (USGA) method. The purpose is to investigate the structural characteristics and thermal stability of such nanocomposites.

2. Experimental Details

An alloy ingot with a composition of $Al_{88}Ni_9Ce_2Fe_1$ (at%) was prepared from induction-melting high-purity constituent elements under an argon atmosphere. Micrometer-sized powders containing nanostructures were prepared by ultrasonic gas atomization (USGA) method. During spray atomization, $Al_{88}Ni_9Ce_2Fe_1$ parent alloy was melted and superheated to 1200°C. The superheated melt was then disintegrated into a stream of micro-sized droplets using helium gas with an atomization pressure of 5.44 MPa. The mass flow-rate of the atomization gas and melt were kept at 0.056 and 0.025 kg/s, respectively. The resulting powders with different size fractions were allowed to cool and sieved in an inert gas atmosphere. To avoid oxidation of the alloy during processing, the experiment was conducted inside an environmental chamber, which was evacuated to below 1 Pa, and back-filled with purified argon gas to a pressure of 100 kPa prior to melting and atomization. The particle size fraction was measured by a Horiba LA-500 laser scattering particle size analyzer. In the

*To whom all correspondence should be addressed: E-mail: aptjong@cityu.edu.hk

Table 1 Three kinds of the as-atomized $Al_{88}Ni_9Ce_2Fe_1$ powder samples studied.

Sample No.	1	2	3
Powder size range (μm)	<10	+10/−25	+25/−40

as-solidified powders, three kinds of samples (1, 2, 3) are separated, of which the particle sizes are listed in Table 1. The powders larger than 40 μm are excluded.

Structural characterization of the as-quenched and as-annealed powder samples was made using a Rigaku X-ray diffractometer (Cu Kα radiation) and a Philips EM420 transmission electron microscope (TEM) with an accelerating voltage of 120 V. The average Al nanocrystal sizes, lattice parameters and microstrains were determined from the broadening of Bragg diffraction, *i.e.* (220), (222) and (422), by using Williamson-Hall method.[10] A polycrystalline Si standard was employed to calibrate the instrumental broadening. Thin foils for TEM observations were prepared from the atomized powders, embedded in electroplated copper matrix. Discs, with diameter of about 3 mm, punched from the resulting powder/copper composite, were mechanically ground and jet electropolished.

Thermal analysis was carried out in a differential scanning calorimeter (Perkin-Elmer DSC-7). The samples, consolidated from the as-atomized powders, were sealed in aluminum pans and scanned at a heating rate of 20°C/min from room temperature up to 600°C, under flowing purified argon. The baseline was obtained by performing a second scan under identical heating conditions. The error in integrated enthalpy release was determined from the standard deviation of several measurements.

3. Results and Discussion

3.1 Structure of as-atomized samples

The atomized $Al_{88}Ni_9Ce_2Fe_1$ alloy powder particles generally exhibit a typical spheroid morphology with little agglomeration. The resulting median diameter, D_{50}, and its standard deviation, $\sigma = D_{84.1}/D_{50}$, a measure of the spread in particle size, are 20 μm and 2.2, respectively. These data indicate the formation of a relatively fine particle, and narrow size distribution of powders.

Figure 1 shows the X-ray diffraction (XRD) patterns of the as-atomized $Al_{88}Ni_9Ce_2Fe_1$ powders with different size fractions. It is apparent in this figure that powder sample 1 has a broad peak maximum located near 38° (indicated by small arrows in Fig. 1). The position and full width at half maximum of this broad peak yield a nearest-neighbor distance of 0.286 nm, and an effective crystalline size of 1.1 nm, respectively. The limited spatial order is a typical behavior of the metallic glasses. However, the broadened diffraction peak, corresponding to fcc-Al nanocrystal, together with some weak diffraction lines (marked by dashed arrows in Fig. 1), are clearly detected in the XRD pattern of sample 2. These diffraction peaks imply the presence of a small amount of $Al_3(Ni, Fe)$ phase. In the case of sample 3, trace amounts of diffraction peaks for $Al_3(Ni, Fe)$ and $Al_{11}Ce_3$ intermetallic compounds as well as α-Al nanocrystals are identified, indicating the coexistence of nanoscale precipitation phases with an amorphous phase. It is generally known that, during the spray atomization, the finer the size of the as-atomized powder, the higher the cooling rate within it is. In this respect, it appears that the microstructure of $Al_{88}Ni_9Ce_2Fe_1$, changing from amorphous to nanocomposite with increasing the size of powder, is closely related to the variation of the cooling rate.

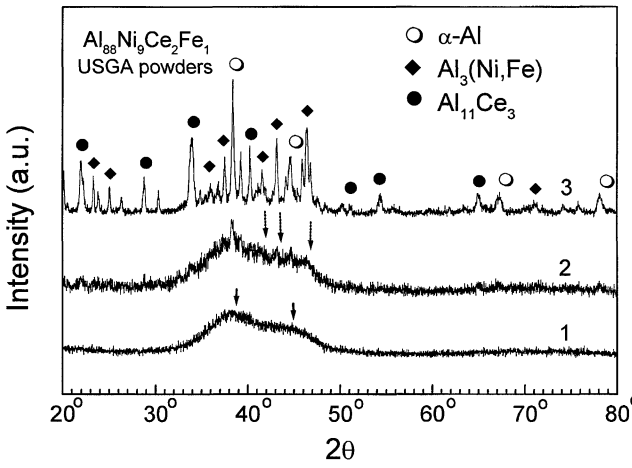

Fig. 1 XRD patterns of the as-quenched $Al_{88}Ni_9Ce_2Fe_1$ powder samples (designated by 1, 2 and 3) with various size fractions.

From the XRD patterns of powder samples 2 and 3, we can determine the average size, d, and microstrain, $\langle e^2 \rangle^{1/2}$, of fcc-Al nanophase precipitated in these powder bands. The results yield d values of 8.1 and 15.1 nm and $\langle e^2 \rangle^{1/2}$ values of ~ 0.22 and 0.13%, respectively. In addition, the calculated values of the α-Al lattice parameter, a, (with an error ± 0.0002 nm) vary from 0.4060 nm for sample 2 to 0.4055 nm for sample 3. These values are larger than the tabulated lattice parameter of pure Al (0.4049 nm). This phenomenon implies that a supersaturated solution containing Ni, Ce and/or Fe in the Al lattice occurs in the as-quenched nanophase composites. Moreover, these results also reveal that the microstructures of the as-atomized powders are affected by nanophase size, microstrain and degree of solute supersaturation, and these essentially vary with the powder size range. Accordingly, the finer particle (sample 2) exhibits a larger degree of solute saturation and microstrain contained, but a smaller size of nanophase precipitated than the coarser one (sample 3).

Figures 2(a)–(b) and 3(a)–(b) show TEM bright and dark field micrographs for the as-atomized powders with different size ranges, respectively. Their corresponding selected area electron diffraction (SAED) patterns are shown in Fig. 2(c) and Fig. 3(c). From TEM images, the internal pores of powders are hardly observed. For sample 2, the SAED pattern and TEM images reveal the presence of the fcc-Al nanocrystallites with random crystallographic orientations, and they are uniformly distributed in the amorphous matrix. Moreover, few faint diffraction rings of intermetallic phase can also be seen in Fig. 2(c). This implies that sample 2 consisting of fcc-Al, amorphous matrix and intermetallic phase. Similarly, the SAED pattern (Fig. 3(c)) indicates that the precipitates formed in sample 3 are $Al_3(Ni, Fe)$ and $Al_{11}Ce_3$ intermetallics as well as fcc-Al nanocrystals. From these TEM mi-

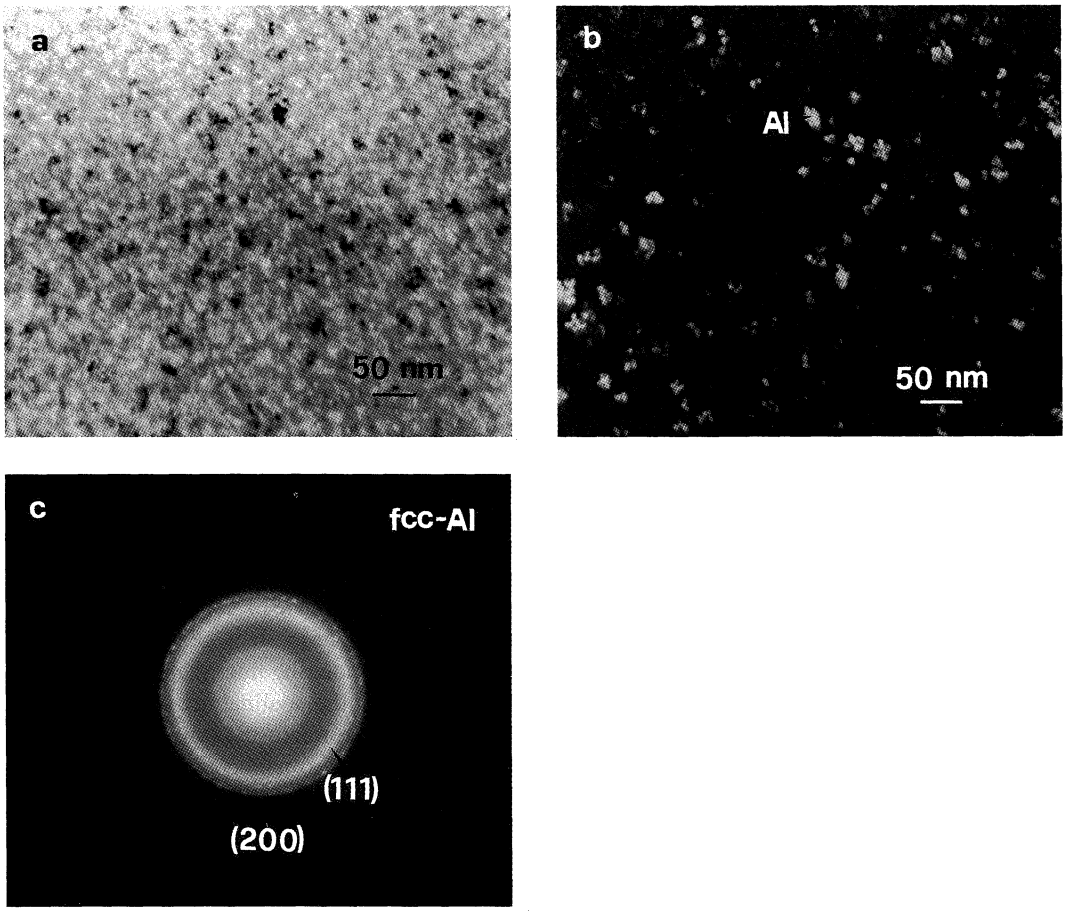

Fig. 2 (a) Bright-field image, (b) dark-field electron micrograph and (c) selected area electron diffraction pattern of the as-quenched $Al_{88}Ni_9Ce_2Fe_1$ powder sample 2.

crographs, also, the size of crystals is measured by means of image analysis. Excluding the crystals that overlapped with each other, every nanoparticle is treated as a sphere having an identical projected area; the equivalent diameter is considered to be the actual precipitation phase diameter. However, some irregular crystals having a dendritic structure can also be seen in TEM images of both samples. The presence of dendritic particles complicates the determination of the size of crystals. From the image analysis, we first estimate the whole area contribute by dendritic particles. And then calculate how large a spherical particle could correspond to such projected area. Figures 4(a)–(d) depict the measured crystal diameter distributions for $Al_{88}Ni_9Ce_2Fe_1$ powders. As crystal diameter is obtained from TEM micrographs, energy dispersive analysis (EDS) is employed to assist the identification of Al, $Al_3(Ni, Fe)$ and $Al_{11}Ce_3$ nanophases during TEM observation. From Fig. 4(a), the measured mean size of fcc-Al crystals is about 8.2 nm for sample 2. The mean sizes of fcc-Al, $Al_3(Ni, Fe)$ and $Al_{11}Ce_3$ nanophases for sample 3 are determined to be 15.2, 10.1 and 9.8 nm, respectively (see Figs. 4(b)–(d)). The results obtained from the TEM are in a good agreement with those from the XRD. Similar cases were also reported by Rizzi *et al.* during the primary crystallization of $Ni_{36}Fe_{32}Ta_7Si_8B_{17}$ and $Al_{90}Ni_6Nd_4$ amorphous phases.[11] Considering the similarity in the formation mechanism of such microstructures by direct quenching and by devitrification, this may be associated with nucleation in the transient regime before reaching a steady state of the nucleation frequency.

Furthermore, the crystal density of the samples 2 and 3 can also be determined from dark-field electron micrographs. Accordingly, the density of the samples 2 and 3 is determined to be 1.08×10^{22} and $3.0 \times 10^{22}\ m^{-3}$, respectively. It should be noted that the nanocrystal density ($\sim 10^{22}\ m^{-3}$) determined from the dark field images is somewhat smaller than the actual number density of crystalline particles. This is because the dark field images are excited using a small portion of diffraction rings. And the nanocrystals are also packed with a certain fraction of the remaining amorphous phase. The actual number density of nanocrystals is in the order of $10^{23}\ m^{-3}$. Since the number of measured crystals is less than the true number, and to compensate for this error, Calin and Köster[4,12] have proposed that the measured numbers can be multiplied with a factor of 4 during primary crystallization studies of Al–Ni–RE (RE = Y, Ce, Nd) metallic glasses. They reported that the nanocrystal nucleation density obtained from such an approximation is in the order of 10^{21}–$10^{23}\ m^{-3}$. This result is confirmed to be reasonable. Consequently, the nanocrystal density of the present samples 2 and 3 is found to be 4.3×10^{22}, $1.2 \times 10^{23}\ m^{-3}$, respectively. Such a large number of nanocrystals ($> 10^{22}\ m^{-3}$), *i.e.*, considerably in excess of the regular populations of heterogeneous sites ($\sim 10^{13}\ m^{-3}$) in metallic melts,[13] together with the size distributions of nanocrystals as discussed-above, make it difficult to form ultrafine microstructures by either spinodal decomposition or heterogeneous nucleation mode. This suggests that the nucle-

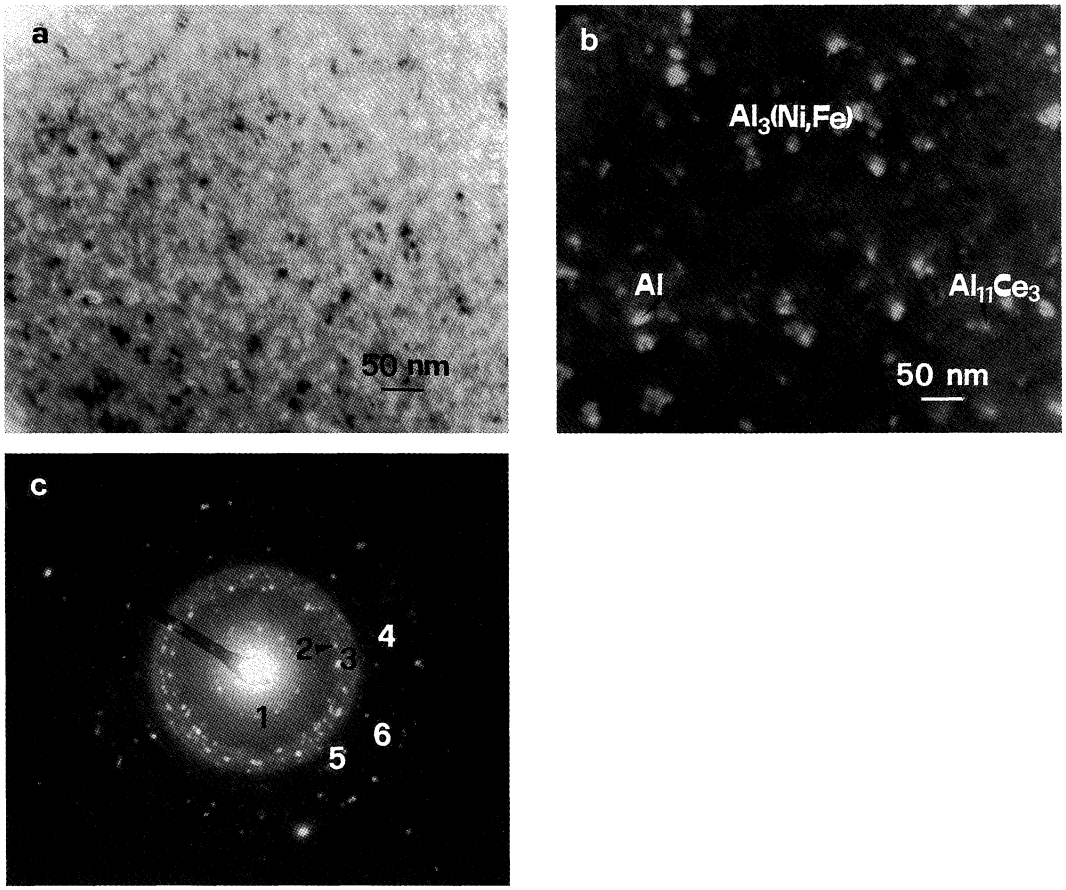

Fig. 3 (a) Bright-field image and (b) dark-field electron micrograph and (c) selected area electron diffraction pattern of the as-quenched $Al_{88}Ni_9Ce_2Fe_1$ powder sample 3. The nanophases marked in (b) are determined by energy dispersive spectra (EDS) analysis. The reflections of rings of 1–6 in (c) are identified to be $(013)_{Al_{11}Ce_3}$, $(111)_{Al}$, $(131)_{Al_3(Ni,Fe)}$, $(200)_{Al}$, $(220)_{Al}$, $(311)_{Al}$, respectively.

ation of nanocrystals is fast, copious and homogeneous.[5,7,14]

3.2 Devitrification behavior

The thermal stability of $Al_{88}Ni_9Ce_2Fe_1$ glassy phase and nanocomposites is investigated by differential scanning calorimetry (DSC) and the results are summarized in Figs. 5(a)–(b). From the DSC heating scan, two exothermic peaks are detected for the three powder samples for which transformation is spreading over a large temperature range. The first peak appearing in the temperature range of 190 to 220°C is associated with the primary crystallization of aluminum. The DSC signal is skewed on the high temperature range. Its shape is similar to that commonly observed in primary crystallization of other alloys where ultrafine crystal is produced, *e.g.*, $Al_{92}Sm_8$, $Al_{88}Y_7Fe_5$, $Al_{88}Gd_8Ni_4$.[5,11,15] DSC heating curve in Fig. 5 does not show the endothermic peak associated with the relaxation of the amorphous phase.

From Fig. 5(b), the second exothermic peak located at ~350°C can be deconvoluted into two separate peaks. A high intensity peak resolved after deconvolution is assigned to the main peak (2 m) whilst a small shoulder peak is assigned to 2 s (Fig. 5(b)). The Gaussian functions are used to fit the deconvoluted peaks, and the standard deviations must be minimized. Thus the onset temperature, T_{o2m}, T_{o2s}, the peak temperature T_{p2m}, T_{p2s} and the heat release ΔH_{2m}, ΔH_{2s} for the respective main and shoulder peaks can be determined accordingly. To understand the origin of the second exothermic peak, XRD measurements of annealed samples 2, at temperatures near the vicinity (340, 360°C) and far from this peak (250, 450°C) were performed. The results are shown in Fig. 6. For the as-solidified powders heated at 250°C, the XRD profile shows the presence of aluminum peaks and an amorphous background. The volume fraction of aluminum is estimated to be ~ 30%. At 340°C, the sample is found to contain mostly aluminum and an $Al_3(Ni, Fe)$ phase. For the sample annealed at 360°C, a trace amount of an $Al_{11}Ce_3$ phase is detected, in addition to sharper diffraction peaks of Al and $Al_3(Ni, Fe)$ phases. Phases formed at 450°C are similar to those at 360°C. In this respect, the occurrence of the second exotherm is attributed to the superimposed growth of $Al_3(Ni, Fe)$ phase in preference to $Al_{11}Ce_3$ phase. A similar behavior is also observed for the other two powder samples with different sizes. This result reveals that rare earth element is more sluggish than other solute elements over the whole crystallization reaction.

The characteristic parameters of the DSC profiles, such as the onset and peak crystallization temperatures, T_{ox}, T_{px}, and heat release, ΔH_x, of two exothermic peaks are indicated in Fig. 5. The measured values of these parameters for different powder sizes are summarized in Table 2. Apparently, the value of T_{o1} for the nanocomposites (samples 2 and 3) is ~ 34 K higher than that of the amorphous powders (sample 1). But only a very small difference (at most 3 K) can be detected for those (T_{o2}, T_{p2}) during the second-step transformation be-

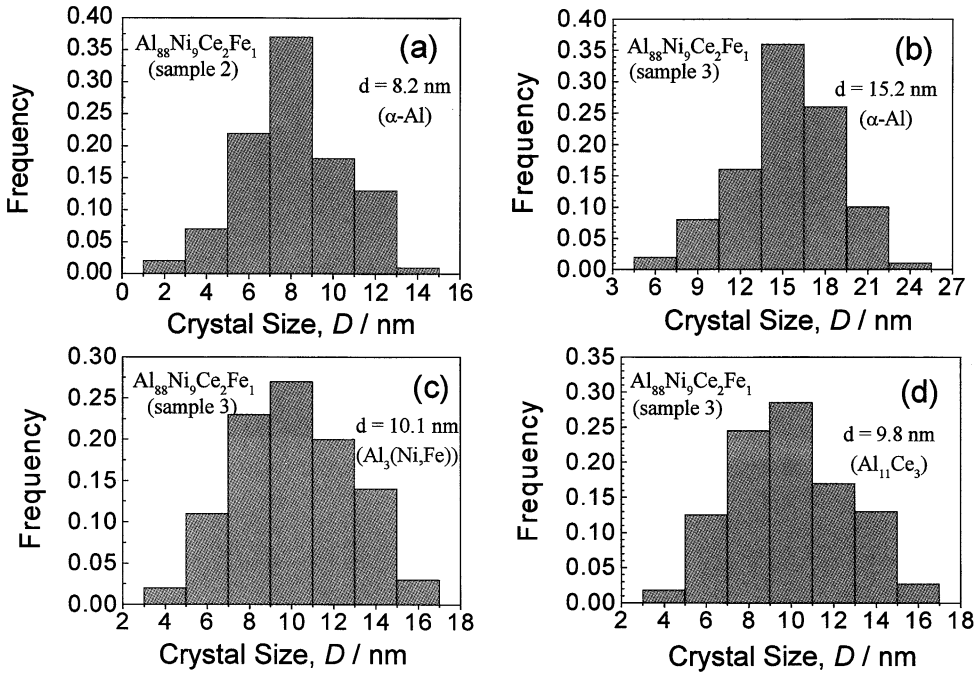

Fig. 4 Measured size distribution of nanocrystals in the as-solidified samples of $Al_{88}Ni_9Ce_2Fe_1$ nanocomposites with (a) sample 2, (b)–(d) sample 3.

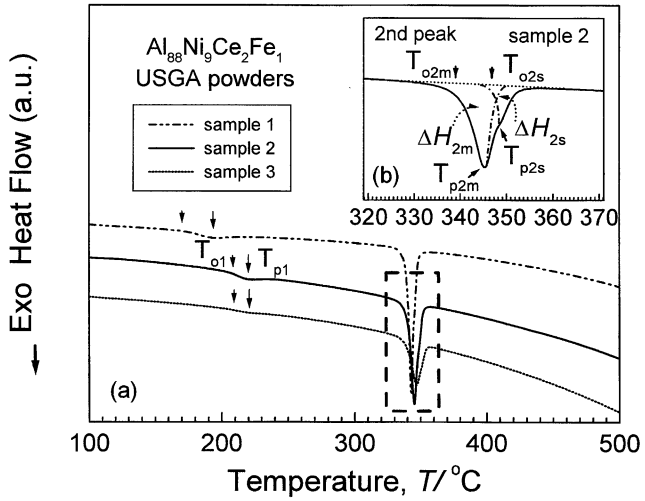

Fig. 5 (a) DSC heating traces showing the crystallization of the as-quenched $Al_{88}Ni_9Ce_2Fe_1$ samples with different size bands. Heating rate of 20°C/min. (b) Separation of the second exothermic peak in DSC. The corresponding crystallization parameters are marked within it.

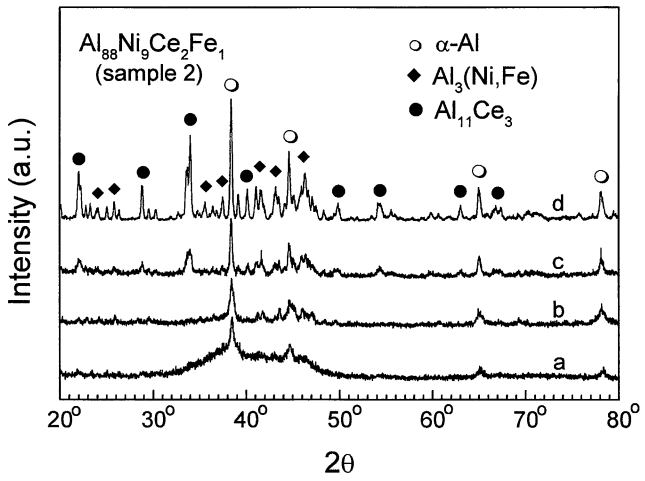

Fig. 6 XRD profiles of powder sample 2 annealed at temperatures of (a) 250°C, (b) 340°C, (c) 360°C, (d) 450°C.

tween the amorphous sample and nanocomposite ones. Moreover, we observed that the heat enthalpies released, ΔH_1, ΔH_{2m} and ΔH_{2s} tend to reduce significantly with increasing the powder size. Suppose volume fraction transformed is proportional to the enthalpy change, from ΔH_1 values as listed in Table 2, we can estimate the residual amorphous fractions, V_{am}, or nanocrystallization fcc-Al transformation fractions, V_f ($= 1 - V_{am}$). As mentioned above, sample 1 with smaller powder size (sub-10 μm) is amorphous, but samples 2 and 3 with larger powder sizes (10–25 and 25–40 μm), consisting of nanocrystallites and amorphous matrix, are referred as the nanocomposites. The V_{am} are determined from the ratio of the value of ΔH_1 of nanocomposites to that of amorphous sample. The measured values of V_f for samples 2 and 3 are 27 and 70%, respectively.

Similar procedures are adopted for ΔH_2 to estimate the volume fractions of intermetallic compounds in these samples. It should be noted that ΔH_2 consists of ΔH_{2m} (main peak) and ΔH_{2s} (shoulder) as shown in Fig. 5(b), which is corresponding to the precipitation process of $Al_3(Ni, Fe)$ and $Al_{11}Ce_3$ nanophase, respectively. Considering that the values of ΔH_{2m} and ΔH_{2s} can also be influenced by the microstrain contained in nanocomposites, the values of microstrain are evaluated from the $\langle e^2 \rangle^{1/2}$, at temperatures surrounding to the two exothermic peaks in DSC traces (at 200, 225, 320 and 350°C). The results yield almost the same values of $\langle e^2 \rangle^{1/2}$ for the two exothermic peaks, *i.e.*, $0.03 \pm 0.02\%$, though a strong microstrain-size-dependence exists in the as-quenched powder samples 2 and 3. This suggests that the variation of ΔH_{2m} and ΔH_{2s} in DSC with the powder size, resulting from the

Table 2 DSC measurement results of the characteristic temperature, T_x (±0.2°C), the average heat release, ΔH_x (±0.04 kJ/mol), and the volume fraction of amorphous phase, V_{am}, for as-atomized $Al_{88}Ni_9Ce_2Fe_1$ metallic glass (sample 1) and nanocomposites (samples 2 and 3), where ΔH_2 is the sum of ΔH_{2s} and ΔH_{2m}. $V_{P\text{-}Al_3(Ni,Fe)}$ and $V_{P\text{-}Al_{11}Ce_3}$ is calculated by the ratio of ΔH_{2m} and ΔH_{2s} of the nanocomposites to those of metallic glass.

Parameter	Sample		
	1	2	3
T_{o1} (°C)	169.6	203.1	204.4
T_{p1} (°C)	190.5	219.6	220.1
T_{o2m} (°C)	338.3	340.9	339.3
T_{p2m} (°C)	342.9	345.7	346.8
T_{o2s} (°C)	243.4	346.3	248.3
T_{p2s} (°C)	345.7	348.5	350.8
ΔH_1 (kJ/mol)	−0.64	−0.47	−0.19
ΔH_2 (kJ/mol)	−2.85	−2.75	−0.99
ΔH_{2m} (kJ/mol)	−1.68	−1.60	−0.56
ΔH_{2s} (kJ/mol)	−1.17	−1.15	−0.43
V_{am} (%)	100	73	30
$V_{P\text{-}Al_3(Ni,Fe)}$ (%)	100	95	33
$V_{P\text{-}Al_{11}Ce_3}$ (%)	100	99	37

microstrain, becomes negligible. Thus, the volume fractions precipitated of $Al_3(Ni, Fe)$ and $Al_{11}Ce_3$ phases for nanocomposites (samples 2 and 3), $V_{P\text{-}Al_3(Ni,Fe)}$ and $V_{P\text{-}Al_{11}Ce_3}$ can be determined from the ratios of ΔH_{2m} and ΔH_{2s} for nanocomposites (samples 2 and 3) to ΔH_2 of amorphous sample 1. Mathematically, they can be expressed as follows,

$$V_{P\text{-}Al_3(Ni,Fe)} = \frac{\Delta H_{2m}^{nc}}{\Delta H_2^{am}} \quad (1)$$

$$V_{P\text{-}Al_{11}Ce_3} = \frac{\Delta H_{2s}^{nc}}{\Delta H_2^{am}} \quad (2)$$

where ΔH_{2m}^{nc} are ΔH_{2s}^{nc} the heat releases for $Al_3(Ni, Fe)$ and $Al_{11}Ce_3$ nanophases of nanocomposites, respectively. ΔH_2^{am} is the heat release for amorphous during the second-step transformation. The calculated results are listed in Table 2. It exhibits a decreasing trend as: 100, 95 to 33% for $V_{P\text{-}Al_3(Ni,Fe)}$ and 100, 99 to 37% for $V_{P\text{-}Al_{11}Ce_3}$ while increasing the powder size. Furthermore, we may infer that, compared with amorphous sample 1, in the as-quenched nanocomposite samples 2 and 3, there are 27 and 70% of fcc-Al nanocrystal ($V_f = 1 - V_{am}$), 5 and 67% of $Al_3(Ni, Fe)$ nanophase ($V_{Q\text{-}Al_3(Ni,Fe)} = 1 - V_{P\text{-}Al_3(Ni,Fe)}$), 1 and 63% of $Al_{11}Ce_3$ nanophase ($V_{Q\text{-}Al_{11}Ce_3} = 1 - V_{P\text{-}Al_{11}Ce_3}$), respectively, which is in good agreement with the XRD result as shown in Fig. 1.

3.3 α-Al nanophase growth kinetics

To understand the thermal stability of $Al_{88}Ni_9Ce_2Fe_1$ nanostructured composites, the α-Al nanophase growth kinetics is investigated in sample 2. Figure 7 shows the isothermal α-Al grain growth behavior at annealing temperatures of 250, 270 and 300°C holding for up to 7.2 ks. It indicates that while samples heated up to the three temperatures, the initial grain size, determined by the XRD, is 13.2, 15.8 and 18.5 nm, respectively. No remarkable growth of α-Al nanophase could be observed at short and long annealing times, indicating its good thermal stability.

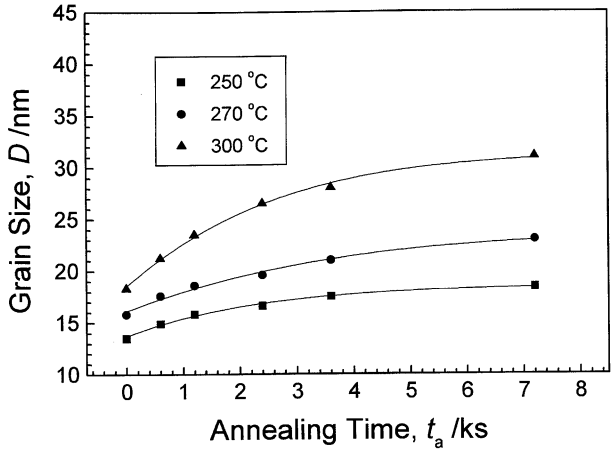

Fig. 7 Annealing time dependence of the grain size at various temperatures for $Al_{88}Ni_9Ce_2Fe_1$ powder sample 2.

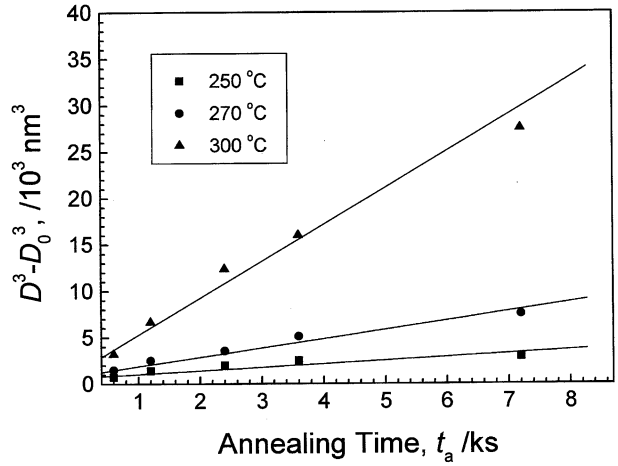

Fig. 8 Variation of $D^3 - D_0^3$ with annealing time (t) for nanocomposite sample 2 at high temperatures, where the slope of linear lines corresponds to the grain growth rate constant.

In general, the grain growth of nanocrystalline materials is primarily driven by an excess energy stored in the grain or interphase boundaries. The most widely used relationship to describe the kinetics of isothermal grain growth is expressed as follows:[16]

$$D^n - D_0^n = kt. \quad (3)$$

Where D_0 and D are the grain sizes at the beginning of the experiment and at time, t, respectively. n is the grain growth exponent. k is a temperature-dependence rate constant, which can be written in an Arrhenius-type equation:

$$k = k_0 \exp(-Q/RT). \quad (4)$$

where Q is the activation energy for isothermal grain growth, R the molar gas constant and k_0 a constant that is independent of the absolute temperature, T. The activation energy, Q, is often used to determine the microscopic mechanism which governs the grain growth.

Accordingly, the growth data of α-Al nanophase in Fig. 7 can be fitted into linear lines with $n = 3$, as indicated in Fig. 8. Moreover, the growth rate constant, k, can be determined from the slope of the lines, which increases from

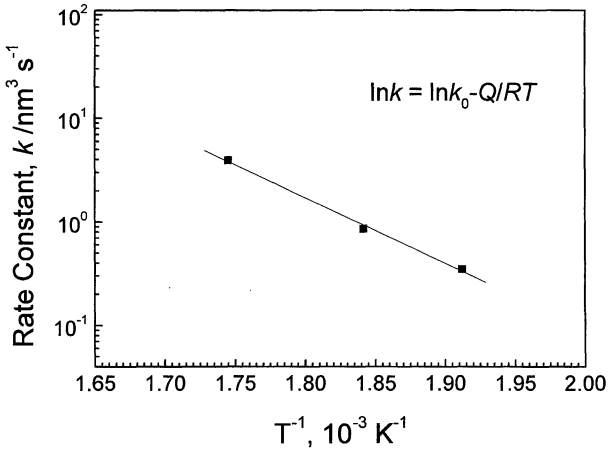

Fig. 9 Arrhenius plot of the grain growth rate constant, $\ln r$, as a function of the reciprocal of the annealing temperature, T, in $Al_{88}Ni_9Ce_2Fe_1$ nanophase composites.

0.35 to 3.96 $nm^3\ s^{-1}$ with increasing temperature from 250 to 300°C. Figure 9 shows the Arrhenius plot of the logarithm of the grain growth rate constant versus the reciprocal of annealing temperature. The plot shows a linear relationship, and the slope yields an activation energy, $Q = 1.3$ eV, for grain growth. The calculated value of Q is close to that for the volume self-diffusion of α-Al (~ 1.5 eV).[17] This indicates that the grain growth behavior, in $Al_{88}Ni_9Ce_2Fe_1$ nanocomposite sample, is associated with the volume-controlled growth. Hono *et al.*[18] have studied the primary crystallization of Al–Ni–Ce alloys by means of the atom probe field ion microscopy. From the atom probe depth profiles, they observed that Ce tends to segregate at the α-Al/amorphous interface. They explain this in terms of the slower diffuivity of Ce than Al and Ni.[18] However, there appears to be no published data on the diffusion coefficient and activation energy of Ce in the Al-TM-Re amorphous alloys. Further work is needed to elucidate the role of Ce diffusion in the Al-TM-Re amorphous alloys.

4. Conclusions

Nano-multiphase $Al_{88}Ni_9Ce_2Fe_1$ materials, with a homogeneous dispersion of nm-sized particles in the amorphous matrix, were produced by gas atomization method. The finer powder particle (10–25 μm) exhibited a larger degree of solute saturation and microstrain, but a smaller size of nanophase precipitated than the coarser one (25–40 μm). In the process of devitrification, there existed a two-stage phase transformation associated with the precipitation of α-Al nanocrystals, and the growth of $Al_3(Ni, Fe)$ nanophase prior to $Al_{11}Ce_3$, respectively. Isothermal annealing treatments of the $Al_{88}Ni_9Ce_2Fe_1$ nanocomposites at temperatures of 250–300°C revealed that α-Al nanocrystal exhibits good thermal stability. Its grain growth kinetics is closely associated with the volume-controlled diffusion mechanism.

Acknowledgements

Financial supports from the National Science Foundation of China (Grant No. 59901011 and 59823001) and the Chinese Academy of Sciences are appreciated. One of the authors (J. Q. Wang) would like to acknowledge the Croucher Foundation of Hong Kong for supporting his visit at City University of Hong Kong. The authors appreciate the helpful discussions with Prof. K. Lu.

REFERENCES

1) Y. H. Kim, A. Inoue and T. Masumoto: Mater. Trans., JIM **31** (1990) 747–749.
2) H. Chen, Y. He, G. J. Shiflet and S. J. Poon: Scr. Metall. Mater. **25** (1991) 1421–1424.
3) X. Y. Jiang, Z. C. Zhong and A. L. Greer: Mater. Sci. Eng. **A226–228** (1997) 789–793.
4) M. Calin and U. Köster: Mater. Sci. Forum **269–272** (1998) 749–754.
5) D. R. Allen, J. C. Foley and J. H. Perepezko: Acta Mater. **46** (1998) 431–440.
6) D. Crespo, T. Pradell, M. T. Clavaguera-Mora and N. Clavaguera: Phys. Rev. **B55** (1997) 3435–3444.
7) K. F. Kelton: Philos. Mag. Lett. **77** (1998) 337–343.
8) K. F. Kelton: Acta Mater. **48** (2000) 1967–1980.
9) Y. Umakoshi, W. Fujitani, T. Nakano, A. Inoue, K. Ohtera, T. Mukai and K. Higashi: Acta Mater. **46** (1998) 4469–4478.
10) G. K. Williamson and W. H. Hall: Acta Metall. **1** (1953) 22–31.
11) P. Rizzi, M. Baricco, G. Riontino and L. Battezzati: Nanostruct. Mater. **11** (1999) 747–755.
12) M. Calin and U. Köster: Mater. Sci. Forum **343–346** (2000) 359–364.
13) J. H. Perepezko: Mater. Sci. Eng. **A65** (1984) 125–135.
14) A. L. Greer: Metall. Trans. **27A** (1996) 549–555.
15) A. K. Gangopadhyay and K. F. Kelton: Philos. Mag. **A180** (2000) 1193–1206.
16) M. J. Mayo: Inter. Mater. Rev. **41** (1996) 85–115.
17) C. J. Smithells: *Smithells Metals Reference Book*, ed. E. A. Brandes and G. B. Brook (Butterworth-Heinemann, London, 1992), Chapter 13, p. 10–11.
18) K. Hono, Y. Zhang, A. Inoue and T. Sakurai: Mater. Trans., JIM **36** (1995) 909–917.